ARTICLES
https://doi.org/10.1038/s41550-020-01295-8

nature astronomy

Check for updates

A tidal disruption event coincident with a high-energy neutrino

Robert Stein[1,2]✉, Sjoert van Velzen[3,4,5]✉, Marek Kowalski[1,2,6]✉, Anna Franckowiak[1,2], Suvi Gezari[4,7], James C. A. Miller-Jones[8], Sara Frederick[4], Itai Sfaradi[9], Michael F. Bietenholz[10,11], Assaf Horesh[9], Rob Fender[12,13], Simone Garrappa[1,2], Tomás Ahumada[4], Igor Andreoni[14], Justin Belicki[15], Eric C. Bellm[16], Markus Böttcher[17], Valery Brinnel[2], Rick Burruss[15], S. Bradley Cenko[7,18], Michael W. Coughlin[19], Virginia Cunningham[4], Andrew Drake[14], Glennys R. Farrar[3], Michael Feeney[15], Ryan J. Foley[20], Avishay Gal-Yam[21], V. Zach Golkhou[16,22], Ariel Goobar[23], Matthew J. Graham[14], Erica Hammerstein[4], George Helou[24], Tiara Hung[20], Mansi M. Kasliwal[14], Charles D. Kilpatrick[20], Albert K. H. Kong[25], Thomas Kupfer[26], Russ R. Laher[24], Ashish A. Mahabal[14,27], Frank J. Masci[24], Jannis Necker[1,2], Jakob Nordin[2], Daniel A. Perley[28], Mickael Rigault[29], Simeon Reusch[1,2], Hector Rodriguez[15], César Rojas-Bravo[20], Ben Rusholme[24], David L. Shupe[24], Leo P. Singer[18], Jesper Sollerman[30], Maayane T. Soumagnac[21,31], Daniel Stern[32], Kirsty Taggart[28], Jakob van Santen[1], Charlotte Ward[4], Patrick Woudt[13] and Yuhan Yao[14]

Cosmic neutrinos provide a unique window into the otherwise hidden mechanism of particle acceleration in astrophysical objects. The IceCube Collaboration recently reported the likely association of one high-energy neutrino with a flare from the relativistic jet of an active galaxy pointed towards the Earth. However a combined analysis of many similar active galaxies revealed no excess from the broader population, leaving the vast majority of the cosmic neutrino flux unexplained. Here we present the likely association of a radio-emitting tidal disruption event, AT2019dsg, with a second high-energy neutrino. AT2019dsg was identified as part of our systematic search for optical counterparts to high-energy neutrinos with the Zwicky Transient Facility. The probability of finding any coincident radio-emitting tidal disruption event by chance is 0.5%, while the probability of finding one as bright in bolometric energy flux as AT2019dsg is 0.2%. Our electromagnetic observations can be explained through a multizone model, with radio analysis revealing a central engine, embedded in a UV photosphere, that powers an extended synchrotron-emitting outflow. This provides an ideal site for petaelectronvolt neutrino production. Assuming that the association is genuine, our observations suggest that tidal disruption events with mildly relativistic outflows contribute to the cosmic neutrino flux.

On 2019 October 1, the IceCube Neutrino Observatory[1] reported the detection of a ~0.2 PeV neutrino, IC191001A, with an estimated 59% probability of being of astrophysical origin solely on the basis of reconstructed energy[2]. Seven hours later, the direction of the incoming neutrino was observed by the Zwicky Transient Facility (ZTF)[3] as part of our neutrino follow-up

[1]Deutsches Elektronen-Synchrotron DESY, Zeuthen, Germany. [2]Institut für Physik, Humboldt-Universität zu Berlin, Berlin, Germany. [3]Center for Cosmology and Particle Physics, New York University, New York, NY, USA. [4]Department of Astronomy, University of Maryland, College Park, MD, USA. [5]Leiden Observatory, Leiden University, Leiden, The Netherlands. [6]Columbia Astrophysics Laboratory, Columbia University in the City of New York, New York, NY, USA. [7]Joint Space-Science Institute, University of Maryland, College Park, MD, USA. [8]International Centre for Radio Astronomy Research—Curtin University, Perth, Australia. [9]Racah Institute of Physics, The Hebrew University of Jerusalem, Jerusalem, Israel. [10]Hartebeesthoek Radio Astronomy Observatory, SARAO, Krugersdorp, South Africa. [11]Department of Physics and Astronomy, York University, Toronto, Ontario, Canada. [12]Astrophysics, Department of Physics, University of Oxford, Oxford, UK. [13]Department of Astronomy, University of Cape Town, Rondebosch, South Africa. [14]Division of Physics, Mathematics, and Astronomy, California Institute of Technology, Pasadena, CA, USA. [15]Caltech Optical Observatories, California Institute of Technology, Pasadena, CA, USA. [16]DIRAC Institute, Department of Astronomy, University of Washington, Seattle, WA, USA. [17]Centre for Space Research, North-West University, Potchefstroom, South Africa. [18]Astroparticle Physics Laboratory, NASA Goddard Space Flight Center, Greenbelt, MD, USA. [19]School of Physics and Astronomy, University of Minnesota, Minneapolis, MN, USA. [20]Department of Astronomy and Astrophysics, University of California, Santa Cruz, CA, USA. [21]Department of Particle Physics and Astrophysics, Weizmann Institute of Science, Rehovot, Israel. [22]The eScience Institute, University of Washington, Seattle, WA, USA. [23]The Oskar Klein Centre, Department of Physics, Stockholm University, AlbaNova, Stockholm, Sweden. [24]IPAC, California Institute of Technology, Pasadena, CA, USA. [25]Institute of Astronomy, National Tsing Hua University, Hsinchu, Taiwan. [26]Kavli Institute for Theoretical Physics, University of California, Santa Barbara, CA, USA. [27]Center for Data Driven Discovery, California Institute of Technology, Pasadena, CA, USA. [28]Astrophysics Research Institute, Liverpool John Moores University, Liverpool, UK. [29]Université Lyon, Université Claude-Bernard Lyon 1, CNRS/IN2P3, IP2I Lyon, Villeurbanne, France. [30]The Oskar Klein Centre, Department of Astronomy, Stockholm University, AlbaNova, Stockholm, Sweden. [31]Lawrence Berkeley National Laboratory, Berkeley, CA, USA. [32]Jet Propulsion Laboratory, California Institute of Technology, Pasadena, CA, USA.
✉e-mail: robert.stein@desy.de; sjoert@nyu.edu; marek.kowalski@desy.de

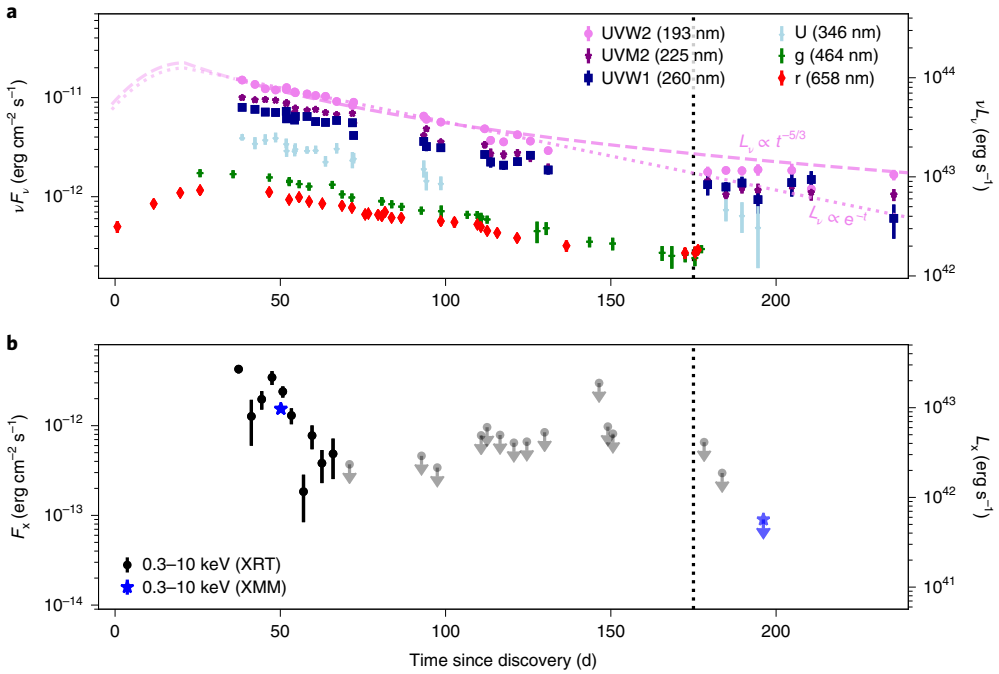

Fig. 1 | Multiwavelength lightcurve of AT2019dsg. a, The optical photometry in bands g and r from ZTF (in green and red, respectively), alongside UV observations in bands UVW2, UVM2, UVW1 and U from the Neil Gehrels Swift Observatory (Swift)-UVOT (Ultraviolet/Optical Telescope) (in pink, violet, navy and blue, respectively). The left axis shows νF_ν, where F_ν is the spectral flux density at frequency ν, while the right axis shows νL_ν, where L_ν is the luminosity at frequency ν. The late-time UV observations show an apparent plateau, which is not captured by a single-power-law decay. The dashed pink line illustrates a canonical $t^{-5/3}$ power law, while the dotted pink line illustrates an exponentially decaying lightcurve. Neither model describes the UV data well. **b**, The integrated X-ray energy flux, from observations with Swift-XRT (X-Ray Telescope) and XMM-Newton, in the energy range 0.3–10 keV. Arrows indicate 3σ upper limits. The vertical dotted line illustrates the arrival of IC191001A. Error bars represent 1σ intervals.

programme. The data were processed by our multimessenger pipeline (Methods), which performs searches for extragalactic transients in spatial and temporal coincidence with high-energy neutrinos[4], and the radio-emitting tidal disruption event (TDE) AT2019dsg was identified as a candidate neutrino source.

TDEs are rare transients that occur when stars pass close to supermassive black holes. Studies have suggested that TDEs are sources of high-energy neutrinos and ultra-high-energy cosmic rays[5–7]; this holds in particular for the subset of TDEs with relativistic particle jets[8–11]. Those TDEs with non-thermal emission are considered the most likely to be sources of high-energy neutrinos. AT2019dsg was thus quickly identified as a promising candidate neutrino source[12]. Given that there are typically $\lesssim$2 radio-emitting TDEs in the entire northern sky at any one time, we find that in the 80 sq. deg. of sky observed during the eight neutrino follow-up campaigns by ZTF up to March 2020 the probability of finding a radio-detected TDE–neutrino association by chance is <0.5%. With the second-highest bolometric energy flux of all 17 TDEs detected by ZTF, the probability of finding a TDE at least as bright as AT2019dsg by chance is just 0.2%. These calculations are valid for any isotropic distribution, and therefore quantify the probability that the AT2019dsg–IC191001A association would arise from atmospheric backgrounds. Our programme targets four neutrino population hypotheses[13], of which the greatest sensitivity is for TDEs (Methods). Thus, although not directly reflected in the calculation, the impact of multiple hypothesis tests on these estimates would be modest. While an atmospheric origin for the IC191001A–AT2019dsg association cannot be excluded, the improbability of chance temporal and spatial coincidence substantially reinforces the independent energy-based evidence of an astrophysical origin for IC191001A, and indicates that any atmospheric origin is unlikely.

AT2019dsg was discovered[14] by ZTF on 2019 April 9, and was classified as a TDE on the basis of its optical spectrum[15] (see Extended Data Fig. 1). This spectrum showed a redshift of $z=0.051$, implying a luminosity distance $D_L \approx 230$ Mpc assuming a flat cosmology with $\Omega_\Lambda = 0.7$ and $H_0 = 70\,\mathrm{km\,s^{-1}\,Mpc^{-1}}$. The optical/UV continuum of AT2019dsg is well described by a single blackbody photosphere with a near-constant temperature[16] of $10^{4.59\pm0.02}$ K and radius of $10^{14.59\pm0.03}$ cm. The peak luminosity of $10^{44.54\pm0.08}$ erg s^{-1} is in the top 10% of the 40 known optical TDEs to date[16], and the temperature is in the top 5%. The late-time evolution is consistent with the rapid formation of an accretion disk[17,18] (Fig. 1), which would be expected on these relatively short timescales for disruptions around higher-mass supermassive black holes. Indeed the total mass of the host galaxy of AT2019dsg is in the top 10% of all optical TDE hosts. Assuming that 50% of the host mass is in the bulge, we estimate[19] a black hole mass of $\sim 3\times10^7\,M_\odot$.

AT2019dsg was also detected in X-rays, beginning 37 d after discovery (Fig 1, see also Extended Data Fig. 2). Though the first X-ray observation indicated a bright source, with a high X-ray to optical ratio of $L_X/L_{opt} \approx 0.1$, this X-ray flux faded extremely rapidly, as shown in Fig. 1. This rate of decline is unprecedented, with at least a factor of 50 decrease in X-ray flux over a period of 159 d. Similarly to the optical/UV emission, the observed X-ray spectrum is consistent with thermal emission, but from a blackbody of temperature $10^{5.9}$ K (0.072 ± 0.005 keV) and, assuming emission from a circular disk, a radius of $\sim 2\times10^{11}$ cm (see Extended Data Fig. 3). As for most X-ray-detected TDEs[20–22], the blackbody radius appears to be much smaller than the Schwarzschild radius ($R_S \approx 10^{13}$ cm) inferred from the galaxy scaling relation[19]. X-ray emission is generally expected to arise close to the Schwarzschild radius. Small emitting areas can arise from an edge-on orientation, because the relativistic velocities at the inner disk can Doppler boost a large area of the disk out

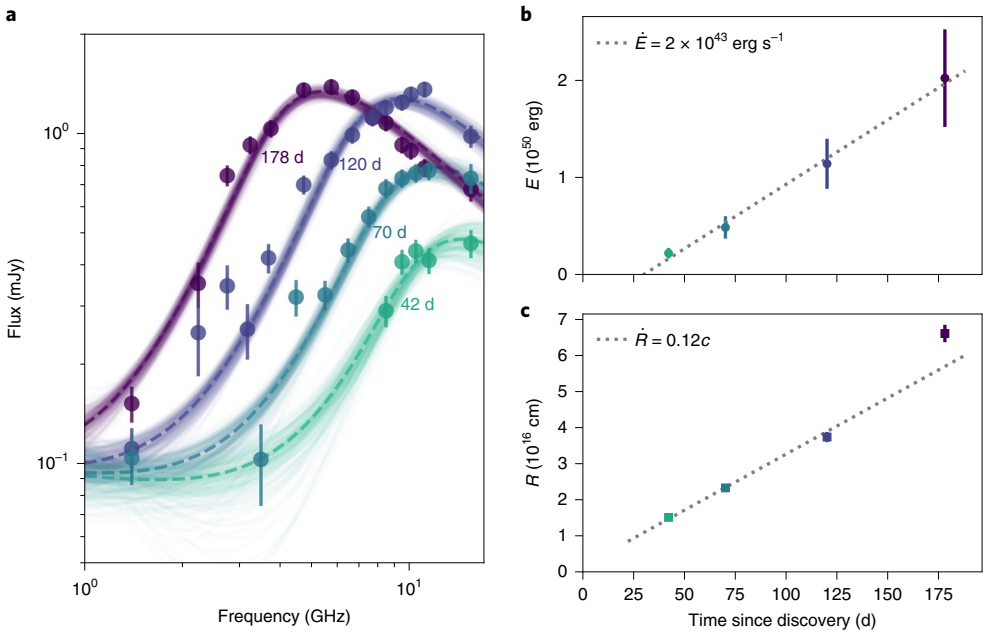

Fig. 2 | Synchrotron analysis of AT2019dsg. a, Radio measurements from MeerKAT (1.3 GHz), the Karl G. Jansky Very Large Array (VLA; 2–12 GHz) and the Arcminute Microkelvin Imager (AMI; 15.5 GHz) at four epochs with times listed relative to the first optical detection. The coloured lines show samples from the posterior distribution of synchrotron spectra fitted to the measurements at each epoch, and the dashed lines trace the best-fit parameters for that epoch. The free parameters are the electron power-law index ($p = 2.9 \pm 0.1$) and the host baseline flux density, plus the magnetic field and radius for each epoch. **b**, The energy at each epoch for a conical outflow geometry with an half-opening angle of 30°. The dotted line indicates a linear increase of energy. **c**, The corresponding radius for each epoch, with a dotted line illustrating a linear increase. Error bars represent 1σ intervals.

of the X-ray band. Since our observations probe close to the Wien tail of the spectrum, a small temperature decrease due to absorption would also yield a substantially underestimated blackbody radius and luminosity[22]. The exponential decrease of the flux could be caused by cooling of the newly formed TDE accretion disk[18] or increasing X-ray obscuration.

Radio observations shown in Fig. 2 reveal a third distinct spectral component, namely synchrotron emission from non-thermal electrons (see also Extended Data Figs. 4 and 5). We model this emission with a conical geometry as expected for outflows (for example jets or winds) that are launched from—and collimated by—the inner parts of flared accretion disks that emit close to the Eddington limit. Given that electrons are typically accelerated with much lower efficiency than protons in astrophysical accelerators[23], we assume that they carry 10% of the energy carried by relativistic protons ($\epsilon_e = 0.1$). We further assume that the magnetic fields carry 0.1% of the total energy ($\epsilon_B = 10^{-3}$), as indicated by radio observations of other TDEs[24] and supernovae[25]. We note that the opening angle for the outflow is largely unconstrained. For a half-opening angle, ϕ, of 30° we find $R = 1.5 \times 10^{16}$ cm in our first epoch (41 d after discovery), increasing to $R = 7 \times 10^{16}$ cm shortly after the neutrino detection (177 d after discovery). These radii scale[26] as $R \propto [1 - \cos(\phi)]^{-8/19}$. The implied expansion velocity is roughly constant at $v/c = \dot{R}/c = 0.12 \pm 0.01$ during the first three epochs, with a significant ($>3\sigma$) acceleration to $v/c = 0.21 \pm 0.02$ for the last epoch. These are the velocities of the synchrotron-emitting region, and thus provide a lower limit to the velocity at the base of the outflow. Indeed even the hotspots of relativistic jets from active galaxies that are frustrated by gas in their host galaxy are typically observed[27] to have subrelativistic expansion velocities of ~0.1 c.

The inferred outflow energy, E, shows a linear increase from 2.5×10^{49} erg to 2×10^{50} erg (Fig. 2), which would not be expected from models of TDE radio emission that involve a single injection of energy[28,29]. The constant increase of energy implies a constant injection rate at the base of the outflow of approximately 2×10^{43} erg s^{-1}. While some scenarios can yield an increase in inferred energy from a single energy injection, none of these are consistent with the full set of observed properties. First, a single ejection with a range of velocities could explain the observed linear increase of energy with time (the slower ejecta arrive later), but is incompatible with the increasing velocity. Second, an increase of the efficiency for conversion of Poynting luminosity to relativistic particles is unlikely because the target density that is available to establish this conversion is decreasing. Finally, an apparent increase of the inferred energy due to an increase of solid angle that emits to our line of sight is only expected for relativistic outflows that decelerate. Instead, for AT2019dsg, the observations suggest the presence of a central engine that yields continuous energy injection through a coupling of accretion power to the radio emission[30], with acceleration in the final radio epoch due to a decrease in the slope of the ambient matter density profile.

Neutrino emission from AT2019dsg

With this strong evidence for three distinct emission zones derived purely from multiwavelength observations, we consider whether this picture is consistent with AT2019dsg being the source of the neutrino IC191001A. In particular, neutrino production requires protons to be accelerated to sufficiently high energies, and to collide with a suitably abundant target. The detection of a single high-energy neutrino implies a mean expectation in the range $0.05 < N_{\nu,\mathrm{tot}} < 4.74$ at 90% confidence, where $N_{\nu,\mathrm{tot}}$ is the cumulative neutrino expectation for all TDEs that ZTF has observed, while for an individual object the expectation will be substantially lower[31]. AT2019dsg emits $f_{\mathrm{bol}} \approx 0.16$ of the population bolometric energy flux, and if we take this as a proxy for neutrino emission we would expect $0.008 \lesssim N_\nu \lesssim 0.76$ for this source.

Radio observations confirm that particle acceleration is indeed occurring, and that this continues without decline until the detection

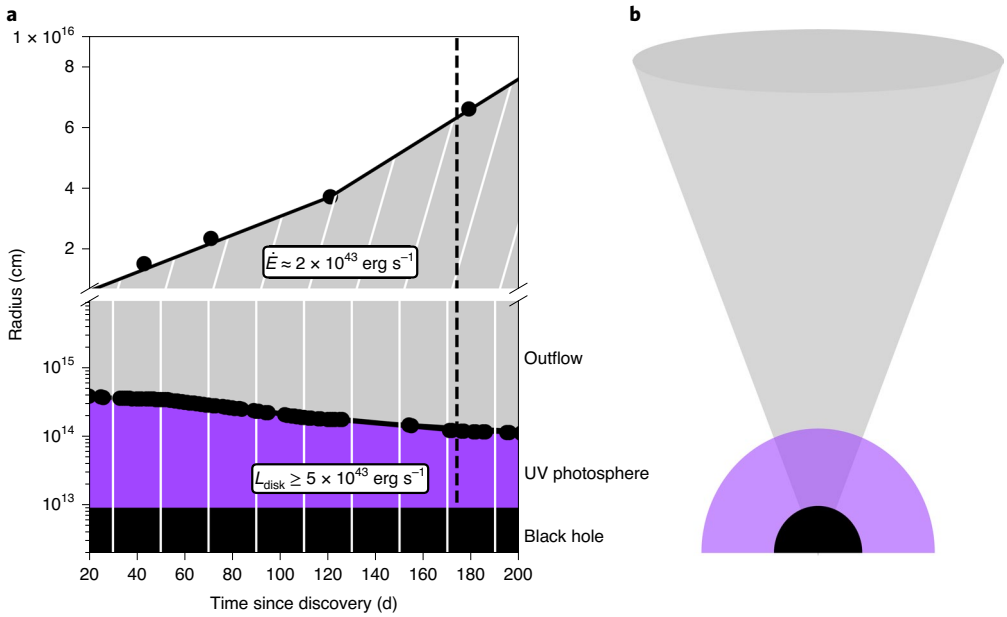

Fig. 3 | Diagram of the three emission zones in AT2019dsg. a, The temporal evolution of the three emission regions. **b**, The geometry of these same regions. The size of the region responsible for radio emission (in grey), as well as the blackbody radius for the UV emission (in purple), is derived from data. The Schwarzschild radius is plotted in black for a black hole mass of $3 \times 10^7 M_\odot$. The white lines in **a** represent a continuous outflow with velocity c.

of the neutrino ~180 d after discovery. Given that neutrinos typically take a fraction $\eta_{p\nu} \approx 0.05$ of the parent proton energy, our accelerator must be capable of accelerating protons to at least 4 PeV. We evaluate the Hillas criterion[32] that the proton Larmor radius be less than the system size, to determine whether this is possible. We use our estimates for conditions in the synchrotron zone at the time of neutrino detection, with $B \approx 0.07$ G and $R \approx 7 \times 10^{16}$ cm for the near-contemporaneous radio epoch. Taking this as a baseline, we find a maximum proton energy of ~160 PeV, far in excess of our requirements. The Hillas criterion can also be satisfied within the engine that powers the radio-emitting outflow, because the product BR is not expected to decrease at smaller radii (for example, $B \propto R^{-1}$ for a toroidal configuration).

The target for neutrino production can be either photons (pγ interactions) or protons (pp interactions). For a photon target, neutrino production occurs above an energy determined by the mass of the Δ resonance, m_Δ. For a thermal spectrum, of temperature T, we then find $\epsilon_\nu \approx \eta_{p\nu}[(m_\Delta{}^2 - m_p{}^2)/4\epsilon_\gamma] \approx 0.3(T/10^5\,\mathrm{K})^{-1}$ PeV. For the UV photosphere of the TDE we find $\epsilon_\nu \approx 0.8$ PeV, while for the compact X-ray source we find $\epsilon_\nu \approx 0.05$ PeV. Both of these values are compatible with the observed neutrino, for which there is a typical uncertainty of one energy decade[33], so either photon field could serve as a target. For the UV photosphere, we find that the mean free path for the parent proton of a petaelectronvolt neutrino ($\sim 2 \times 10^{13}$ cm, Supplementary Information) is much smaller than the photosphere radius, so the UV photosphere is indeed optically thick. At smaller radii, the X-rays would overtake the UV photons as dominant scattering targets.

In the multizone model, shown in Fig. 3, the thermal photons provide a guaranteed target for pion production. However, hadrons could in principle also serve as a target, leading us to consider a single-zone scenario in which the protons are accelerated at the same location as the synchrotron-emitting electrons, with the neutrino spectrum following the same intrinsic energy power law as the protons and electrons. For pp neutrino production, high target densities of $n_p \approx 1/(\sigma_{pp} R) \approx 10^8\,\mathrm{cm}^{-3}$ would be required for efficient production of neutrinos, where σ_{pp} is the proton–proton cross section and $R \approx 10^{17}$ cm is the characteristic size of the radio region at the time of neutrino production. This high density could be provided by the unbound stellar debris, although this component moves with a typical maximum velocity[29] of 0.05 c, and therefore the majority of this debris would have to be swept up with the outflow. Alternatively, the density could be provided by pre-existing gas, although since this gas orbits in the sphere of influence of the black hole it would be challenging to satisfy the upper limits on predisruption accretion.

To obtain the expected neutrino flux from this source we have to estimate the energy (E_p) carried by protons that are accelerated above the energy threshold needed to produce high-energy neutrinos. The outflow energy of 2×10^{50} erg that we derived from the radio observations (Fig. 2) represents a lower bound to the energy that is available for particle acceleration in a central engine. Indeed, the total energy budget for a TDE is set by the mass of the disrupted star, with $E_{TDE} \approx (1/2)0.1\,M_\odot c^2 \approx 10^{53}$ erg for a solar-mass star. We will assume that 1% of this total energy budget is carried by relativistic protons, $E_p \approx 10^{51}$ erg. The total energy in muon neutrinos would then be $E_{\nu,tot} = (1/8)E_p \approx 10^{50}$ erg for efficient optically thick pion production, after accounting for the pion decay yield and subsequent neutrino flavour oscillations. Convolving this implied energy $E_{\nu,tot}$ with the effective area, A_{eff}, of IceCube's high-energy neutrino alert selection[34], we estimate the expected number of neutrino alerts. Approximating the sharply peaked pγ neutrino spectrum as a monoenergetic flux anywhere in the range $0.2\,\mathrm{PeV} \lesssim \epsilon_\nu \lesssim 1$ PeV, we find $N_\nu = (E_{\nu,tot}/\epsilon_\nu)(A_{eff}/4\pi D_L{}^2) \approx 0.03$. Thus any optically thick pγ scenario would be sufficient to produce the neutrino under these assumptions.

In contrast to a peaked pγ neutrino spectrum, for pp production the neutrinos would instead follow a power law. Many of these neutrinos would then fall below the threshold of IceCube's alert selection. The associated gamma rays would however fall within the sensitive range of gamma-ray telescopes, so this scenario could be securely identified through a joint neutrino–gamma-ray signal. While no gamma-ray emission was measured using the Fermi Large Area Telescope (Fermi-LAT) for AT2019dsg (see Methods and

Extended Data Figs. 6–8), gamma-ray Cherenkov telescopes may be sensitive to the expected gamma-ray signal, and the corresponding low-energy (TeV) neutrino emission could confirm a hadronic origin. Conversely, the high optical depth of the UV photosphere would absorb any gamma rays accompanying $p\gamma$ neutrino emission[10]. Some contribution from gamma-dark sources is required to explain the large astrophysical neutrino flux[35].

Given the different neutrino spectrum expectations, a search for accompanying lower-energy neutrinos could be used to probe the conditions at the site of proton interaction. IceCube has already searched for correlations between a sample of TDEs and a neutrino dataset dominated by lower-energy events, and reported that thermal TDEs account for less than 39% of the diffuse astrophysical flux under the assumption of standard candles following a power-law spectrum[36]. The detection of a single TDE–neutrino association with our programme would imply that at least 3% of the astrophysical neutrino alerts arise from the TDE population, fully compatible with these pre-existing limits (Supplementary Information).

As TDE discovery rates have increased substantially since the previous IceCube analysis[16,36], future searches will be able to study neutrino emission from TDEs with much greater sensitivity. A measurement of $O(\sim 1–10)$ TeV neutrinos without accompanying gamma rays would indicate that neutrino production is occurring in the X-ray photosphere, rather than in the UV photosphere. Indeed, such a detection would confirm the presence of a hidden X-ray source in the first place, while our electromagnetic observations cannot. Conversely, a lack of complementary low-energy neutrinos and gamma rays implies that only UV photons serve as a target. Neutrinos can uniquely serve as probes of the inner region of TDEs, using this novel method of extragalactic neutrino tomography. Now that a persistent central engine has been revealed in coincidence with a high-energy neutrino, we can begin to shed light on the role of TDEs as astrophysical accelerators.

Methods

ZTF neutrino follow-up. ZTF routinely images the visible Northern Sky once every three nights to a median depth of 20.5^m, as part of a public survey[3,13]. For our neutrino follow-up programme, this wide-field cadence is supplemented by dedicated Target-of-Opportunity (ToO) observations scheduled through the GROWTH (Global Relay of Observatories Watching Transients Happen) ToO Marshal[37].

With ZTF, we have followed up eight neutrinos in the period from survey start on 2018 March 20 to 2020 March 31, out of a total of 31 neutrino alerts published by IceCube (Supplementary Table 1). From 2019 June 17, IceCube published neutrino alerts with improved selection criteria to provide an elevated alert rate[34]. In addition to 1 of the 12 alerts under the old selection, ZTF followed up 7 of the 19 alerts published under the new selection. In general, we aim to follow all well localized neutrinos of likely astrophysical origin reported by IceCube that are visible to ZTF and can be observed promptly. Those alerts not observed by ZTF are summarized in Supplementary Table 2. Of those 23 alerts not followed up by ZTF, the primary reasons were proximity to the Sun (8/23), alerts with poor localization and low astrophysical probability (6/23) and alert retraction (4/23). For events that were reported with estimates of astrophysical probability, we chose not to follow up those that had both low astrophysical probability (<50%) and large localization regions (>10 sq. deg.). This astrophysical probability was not reported for high-energy starting events under the old IceCube alert selection, or for one recent alert, IC200107A, that was identified outside the standard alert criteria[38].

Each neutrino localization region can typically be covered by one or two ZTF observation fields. Multiple observations are scheduled for each field, with both g and r filters, and a separation of at least 15 min between images. These observations typically last for 300 s, with a typical limiting magnitude of 21.0^m. ToO observations are typically conducted on the first two nights following a neutrino alert, before swapping to serendipitous coverage as part of the public survey. Following observations, images are processed by IPAC[39], and alert packets are generated for significant detections from difference images[40].

This alert stream of significant detections is then filtered by our follow-up pipeline built within the AMPEL framework[41], a platform for realtime analysis of multimessenger astronomy data[42]. Our selection is based on an algorithm for identifying extragalactic transients[42]. We search ZTF data both preceding and following the arrival of the neutrino. To identify candidate counterparts to the neutrino, we apply the following cuts to ToO and survey data.

- We reject likely subtraction artefacts using machine learning classification and morphology cuts[43].
- We reject moving objects through matches to known nearby solar system objects[39]. We further reject moving objects by requiring multiple detections for each candidate (that is, at the same location) separated temporally by at least 15 min.
- We remove stellar sources by rejecting detections cross-matched[44] to objects with measured parallax in Gaia Data Release 2 data[45], defined as non-zero parallax with a significance of at least 3σ. We further reject likely stars with machine learning classifications[46], based on sources detected by Pan-STARRS1[47], removing those objects with an estimated stellar probability greater than 80%.
- We identify likely active galactic nuclei (AGNs) by cross-matching to the Wide-field Infrared Survey Explorer survey and applying IR colour cuts[48]. We reject detections consistent with low-level AGN variability.
- We require that objects lie within the reported 90% error region to ensure spatial coincidence, and that they are detected at least once following the neutrino arrival time to ensure temporal coincidence.

These cuts typically yield ~0.2 candidates per square degree of sky. Promising candidates are prioritized for spectroscopic classification, to confirm or rule out a possible association with a given neutrino.

AT2019dsg (RA[J2000] = 314.26°, dec.[J2000] = +14.20°) was spatially coincident with the 90% localization of the neutrino IC191001A[2] (RA = $314.08^{\circ}{}^{+6.56^{\circ}}_{-2.26^{\circ}}$, dec. = $+12.94^{\circ}{}^{+1.50^{\circ}}_{-1.47^{\circ}}$), at a distance of 1.27° from the best-fit position. It was also temporally coincident, being detected by ZTF in our ToO observations following the neutrino detection. There were additionally three candidate supernovae found in the error region of IC191001A, consistent with background expectations. AT2019dsg was the first TDE identified by our pipeline, and the first TDE to be reported in coincidence with any high-energy neutrino.

Probability of chance coincidence. During the first 18 months of survey operations, ZTF identified 17 TDEs[16], distributed over 28,000° of observed sky (the ZTF survey footprint, after removing sources with a Galactic latitude $|b| < 7$). Of these TDEs, each was typically detected for ~6 months (ref. [16]). We thus estimate that the density of ZTF-detected TDEs is approximately 2.0×10^{-4} per square degree of sky in the survey footprint at any given time. Our follow-up pipeline requires that any candidate be detected by ZTF in ToO observations following a neutrino, to establish temporal coincidence. We assume that our neutrino pipeline does not have a substantially higher selection efficiency than the dedicated ZTF programme to identify TDEs[16], and thus that the latter provides a reasonable estimate of the background rate of TDEs passing our pipeline.

Those TDEs with radio detections are considered the most promising candidates for neutrino production, as the radio emission serves as a tracer for the particle acceleration required in neutrino sources. We can consider the fraction of TDEs that would additionally be detected in radio, assuming that all could be observed. Among the ZTF sample of confirmed TDEs, we undertook radio follow-up observations with the VLA for six, of which two were detected. Taking this implied radio-emitting fraction of 33%, we then find a final density of 5.9×10^{-5} radio-emitting TDEs per square degree of surveyed sky.

ZTF has followed up eight neutrinos up to January 2020, and has covered a combined localization region of 81.05 sq. deg. (Supplementary Table 1). With this sky area, the expected number of coincident radio-detected TDEs across all of our neutrino follow-up campaigns is 4.8×10^{-3}. The Poisson probability of observing at least one radio-emitting TDE during our entire neutrino follow-up campaign is thus 4.8×10^{-3}.

As radio follow-up observations of ZTF TDEs were biased towards those most likely to be detectable, this estimate is an overly conservative one. Because the bolometric energy flux derived from UV/optical observations (that is, the blackbody luminosity over the square of the distance) serves as a proxy for the non-thermal emission, TDEs that were bright under this metric were preferentially selected for radio observations. To avoid this selection bias, we can instead directly use this bolometric energy flux as a proxy for neutrino flux to identify the most promising candidates for neutrino detection, namely those TDEs that are both nearby and luminous. Of the 17 TDEs observed by ZTF, AT2019dsg ranks second in this metric. The probability of finding a TDE in our neutrino follow-up campaign with a bolometric energy flux that is at least as high as AT2019dsg is thus 1.9×10^{-3}.

Like most other studies in neutrino astronomy[33,49], these chance coincidence probability estimates do not account for the so-called 'look-elsewhere effect' from multiple possible hypotheses. In our case, the ZTF programme has sensitivity to four theoretically motivated neutrino population hypotheses (TDEs, core-collapse supernovae, gamma-ray bursts and AGN flares)[13]. The impact of testing multiple hypotheses is thus modest, and a chance coincidence explanation for AT2019dsg–IC191001A remains unlikely.

Of these four, it should also be noted that TDEs are the one to which our programme is most sensitive. As detailed in Supplementary Information, follow-up programmes are generally most effective in identifying neutrino emission from TDEs, since this flux should be dominated by nearby sources, which can be detected by telescopes such as ZTF. Moreover, given their low rate, any individual TDE–neutrino association will be easier to identify than that for more abundant populations such as AGNs or supernovae. TDEs also evolve sufficiently slowly to

enable extensive photometric and spectroscopic follow-up, in marked contrast to fast transients such as gamma-ray burst afterglows, leading to a higher detection efficiency.

Optical/UV observations. Before the detection of IC191001A, AT2019dsg had already been repeatedly detected by the ZTF P48 telescope as part of the public Mid-Scale Innovations Program (MSIP) survey, most recently on 2019 September 28. These data were supplemented by photometric observations from the 2 m Liverpool Telescope[50] and Spectral Energy Distribution Machine[51,52] photometry[53] obtained using the P60 telescope at Palomar Observatory. ToO observations of the neutrino localization field began on 2019 October 1, 7.4 h after the neutrino detection. A second set of observations was performed the following night. In all of these images AT2019dsg was clearly visible.

UV observations of AT2019dsg were conducted as part of a systematic survey of UV properties of all ZTF-identified TDEs[54], using the UVOT[55] on board Swift[56]. Data were reduced with uvotsource using an aperture of 7″ to capture the entire galaxy (the host flux density was subtracted on the basis of the best-fit galaxy model[54] and uncertainties on this baseline are propagated into the reported UVOT difference photometry). The first UV observation was performed 15 d after the optical peak on 2019 May 17, and a bright source spatially coincident with the TDE was detected. Subsequent observations continued at a cadence of 2–3 d, up to 2019 September 7. In this period, AT2019dsg continued to steadily dim. An additional observation occurred shortly before the neutrino detection on 2019 September 27. Follow-up observations were then triggered by the identification of a possible association with IC191001A[12], beginning on 2019 October 5.

The optical/UV data are summarized in Supplementary Table 3. We note that in the final ZTF observations the source appears to redden in the optical bands. This could be a signature of reverberation due to emission from dust heated by the TDE[57,58]; this dust can reach a temperature of ~2,000 K. An important caveat is that the contrast between the transient emission and the host is very small for these late-time optical detections, so the residuals in the difference image may need to be corrected to account for small systematic offsets. This can only be investigated when the images for this portion of the public survey are published as part of the next ZTF data release. We note that the UV observations are not subject to the same uncertainty, because even at late times the transient UV flux is about an order of magnitude brighter than the host baseline.

AT2019dsg was first classified as a TDE by ePESSTO+ on on 2019 May 13 (ref. [15]), and the redshift of AT2019dsg was measured to be $z=0.051$. Further high-resolution spectroscopic observations were conducted using the De Veny Spectrograph on the 4.3 m Lowell Discovery Telescope (LDT, principal investigator (PI) S. Gezari), the Kast Double Spectrograph on the 3 m Lick Observatory Shane Telescope (Lick, PI R.J.F.)[59] and the Low Resolution Imaging Spectrograph on the 10 m Keck Telescope (Keck, PI M.J.G.)[60], with the most recent spectrum on 2019 September 25. These spectra confirm that AT2019dsg belongs to the common spectroscopic class of TDEs with Bowen fluorescence emission lines and broad Hα emission lines[16]. We note that the Ca triplet is also clearly visible in our late-time spectra (rest-frame 8,498 Å, 8,542 Å and 8,662 Å), so the supermassive black hole mass could in principle be inferred more precisely using higher-resolution spectroscopy of this feature[61]. Following the identification of AT2019dsg as a candidate neutrino source, additional high-resolution spectra of the source were taken with the 200″ Hale Telescope Double Spectrograph at Palomar Observatory (P200, PIs M.M.K. and S. R. Kulkarni) on 2019 October 3 and again with Lick on 2019 October 5 and 2019 October 29 (Extended Data Fig. 1). There is no evidence of any significant spectral evolution between these spectra and the most recent preneutrino spectrum from 2019 September 25, and the spectral evolution of AT2019dsg is consistent with that of other TDEs[16].

X-ray observations. AT2019dsg was first observed in X-rays on 2019 May 17 by the XRT[62], also on board Swift[56], as part of a programme to categorize the X-ray properties of TDEs. AT2019dsg was detected at high significance at this epoch, with a measured energy flux of $F_X \approx 4\times10^{-12}$ erg cm^{-2} s^{-1} (0.3–10 keV). Observations continued with a cadence of 2–3 d, and indicated a sharply declining X-ray flux (Supplementary Table 4). The source was last detected on 2019 June 14, and not detected again in any of the subsequent observations continuing until 2019 September 7. An additional observation was performed with the X-ray Multi-Mirror Mission (XMM)-Newton telescope on 2019 May 30, in the range 0.3–10 keV. The XMM-Newton EPIC-pn observations (programmes 082204 and 08425; PI S. Gezari) were taken in Wide window Thin1 filter mode and reduced using standard techniques with the XMM-Newton[63] Science Analysis System (SAS). The source extraction region was a circle of radius 35 arcsec at the location of the optical transient in the X-ray image, and the background was measured using a 108 arcsec circular region (Extended Data Fig. 2). The XMM spectrum was binned using the GRPPHA command, such that there were at least 20 counts contained in each bin. It was then fitted (χ^2/d.f. = 59.26/65) with the disk blackbody (diskbb) model with Galactic[64] and intrinsic ($N_H \approx 4\times10^{20}$ cm^{-2}) absorption described using the phabs model in XSPEC v12.9.1 (ref. [65]). The flux was consistent with those of Swift-XRT, and provided a high-signal-to-noise X-ray spectrum well fitted with a single disk temperature of $T_{disk} = 10^{5.9}$ K (0.072 ± 0.005 keV), shown in Extended Data Fig. 3. Following the identification of AT2019dsg as a candidate counterpart to IC191001A (ref. [12]), additional X-ray observations were triggered. AT2019dsg was again not detected, with the first Swift-XRT observation occurring on 2019 October 5. An additional XMM observation on 2019 October 23 yielded a deep upper limit of 9×10^{-14} erg cm^{-2} s^{-1} (0.3–10 keV) using the same thermal model, computed at the 3σ confidence level using the XMM SAS/HEASARC command eregionanalyse.

Radio observations. Four observations of AT2019dsg were performed with the VLA under project code 19A-395 (PI S.v.V.), on 2019 May 22, June 19, August 8 and October 5. The array was in its moderately extended B configuration (maximum baseline 11 km) for the first two epochs, and in its most extended A configuration (maximum baseline 36 km) for the final two epochs. Our first epoch, on May 22, was a detection experiment, and we observed only in the 8–12 GHz band. Having established the presence of radio emission, we observed over a broader range of frequencies in the subsequent three epochs, using the 2–4 GHz, 4–8 GHz and 8–12 GHz bands. We used 3C 48 as a bandpass and flux-density calibrator on May 22, and 3C 286 for the other three epochs. We used the nearby extragalactic sources International Celestial Reference Frame (ICRF) J204945.8+100314 (at 4–8 and 8–12 GHz) and ICRF J203533.9+185705 (at 2–4 GHz) to determine the complex gain solutions, which were interpolated to AT2019dsg. We used the VLA pipeline to perform external gain calibration, and after removing residual radiofrequency interference we imaged the data within the Common Astronomy Software Application (CASA), using Briggs weighting with a robust parameter of 1. We split each baseband into multiple frequency bins for imaging (1 GHz bins above 4 GHz, and 0.5 GHz bins below this) to provide better sampling of the broadband spectrum, allowing more precise constraints on the turnover frequency, and better spectral modelling.

Radio observations of the field of AT2019dsg were also conducted using the AMI Large Array (AMI-LA)[66,67]. AMI-LA is a radio interferometer comprised of eight 12.8-m-diameter antennas producing 28 baselines that range from 18 m to 110 m, which operates with a 5 GHz bandwidth around a central frequency of 15.5 GHz. We observed AT2019dsg on several epochs (Supplementary Table 5) for 4 h each. Initial data reduction, editing and calibration of the phase and flux density was carried out using reduce_dc, a customized AMI data reduction software package[68]. Phase calibration was conducted using short interleaved observations of ICRF J205135.5+174336, while for absolute flux-density calibration we used 3C 286. Additional flagging and imaging were performed using CASA[69]. All of our observations showed a source consistent with the location of AT2019dsg. We used the CASA task IMFIT to find the source flux and position.

Further observations of AT2019dsg were conducted with the South African MeerKAT telescope, on 2019 June 19, July 29, October 5 and November 30, with each session being ~2 h long. We used ICRF J193925.0−634245 as a flux-density calibrator, and ICRF J213032.8+050217 as a phase and amplitude calibrator. The initial calibration was done using the IDIA MeerKAT pipeline (https://idia-pipelines.github.io/docs/processMeerKAT), which is implemented in CASA. The observed band was 860 MHz wide and centred on 1,280 MHz. We imaged the whole primary beam (~1°) using the CLEAN algorithm (CASA: tclean) to remove sidelobes from the many (unrelated) sources within the primary beam. The total CLEAN flux density in the field was ~1 Jy, and the peak brightness in the images was about 48 mJy per beam (not related to AT2019dsg). Since residual small calibration errors dominated the root mean square background in the initial images, we self-calibrated the data in both phase and amplitude, with the mean amplitude gain being fixed at unity to minimize any drifting of the flux-density scale. The resolution is slightly different in each epoch, but was ~11″ north–south, and ~6″ east–west. Root mean square image background levels also varied, ranging between 25 and 32 μJy per beam. There was no sign of extended emission or confusing sources near AT2019dsg. The flux density was determined by fitting an elliptical Gaussian with the same geometry as the restoring beam to the images.

The measured flux densities from our radio observations are reported in Extended Data Fig. 4. For all radio observations, the reported uncertainties include both the root mean square image background and a 5% fractional calibration uncertainty, added in quadrature.

Gamma-ray observations. We analysed data from the Fermi-LAT[70], sensitive to gamma rays with energies from 20 MeV to greater than 300 GeV. During its sky-survey operations, the pair-conversion telescope Fermi-LAT scans the entire sky about every 3 h, and can monitor the variable gamma-ray sky over short and long timescales. We studied the region of AT2019dsg in three different time intervals, motivated by the multiwavelength behaviour of the source. The first interval (G1) includes 130 d of observations that include the peak of the optical emission from 2019 April 4 to 2019 August 12. The second one (G2) spans 2019 August 12 to 2019 November 20 and covers the apparent UV plateau and the peak of the radio emission. The third period (G3) integrates the whole period between the start of G1 and 2020 January 31. We use the photon event class from Pass 8 Fermi-LAT data (P8R3_SOURCE), and select a 15° × 15° region of interest centred on the AT2019dsg position derived from optical observations, with photon energies from 100 MeV to 800 GeV. We use the corresponding LAT instrument response functions P8R3_SOURCE_V2 with the recommended spectral models gll_iem_v07.fits and iso_P8R3_SOURCE_V2_v1.txt for the Galactic diffuse and

isotropic components respectively. To minimize contamination from gamma rays produced in the Earth's upper atmosphere, we require an instrumental zenith angle $\theta < 90°$ for all events, in addition to the standard data quality cuts suggested by the Fermi Science Support Center (https://fermi.gsfc.nasa.gov/ssc/data/analysis/scitools/data_preparation.html). We perform a likelihood analysis, binned spatially with 0.1° resolution and 10 logarithmically spaced bins per energy decade, using the Fermi-LAT ScienceTools package (fermitools v1.0.1) along with the fermipy package v0.17.4 (ref. [71]).

A search had already performed been within the 90% error region during both the 1 d and 1 month periods before the arrival of the high-energy neutrino[72]. No new gamma-ray source was identified, and there was no significant ($\geq 5\sigma$) detection for any source from the fourth Fermi-LAT point-source catalogue (4FGL[73]). Here, we specifically test a point-source hypothesis at the position of AT2019dsg under the assumption of a power-law spectrum. We find TS = 0 for all intervals, where TS is twice the difference in the maximum log $\mathcal{L}$ of a region of interest model with and without the source, where $\mathcal{L}$ is the likelihood of the data given the model. Upper limits for the energy flux (integrated over the whole analysis energy range) have been derived for a power-law spectrum ($\mathrm{d}N/\mathrm{d}E \propto E^{-\Gamma}$) with photon power-law index $\Gamma = 2$ and are listed in Extended Data Fig. 7, along with the respective time intervals.

In all three time intervals, we detect a new, non-catalogued gamma-ray emitter in the region of interest at a significance of $\geq 5\sigma$. This source lies just outside the IC191001A 90% error region, as indicated in Extended Data Fig. 6. The source, which we label Fermi-J2113.8+1120, is probably the gamma-ray counterpart of the radio-loud object GB6 J2113+1121, classified as a flat-spectrum radio quasar with redshift $z = 1.63$ (ref. [74]). The detection of an unrelated gamma-ray blazar within the neutrino uncertainty area is consistent with the background estimation. On average 1.5 4FGL gamma-ray blazars are expected in 20 sq. deg. A lightcurve analysis (Extended Data Fig. 8) reveals that the source was last detected in gamma rays a month before the IC191001A detection, and was not significantly detected again until another month after the neutrino detection. These results are compatible with the findings of the realtime follow-up of the region, which found no evidence for emission on timescales of 1 d and 1 month before the detection of IC191001A[75].

Such a long apparent lag between gamma-ray emission and neutrino emission is disfavoured by recent studies on the temporal behaviour of hadronic processes in blazars[76,77], suggesting that the blazar is unlikely to have produced the neutrino. Hence, given the lack of any obvious connection between the gamma-ray observations of Fermi-J2113.8+1120 and IC191001A, we do not discuss this source any further.

The HAWC observatory also reported a search for transient gamma-ray emission on short timescales in the localization of IC191001A[78], and set a limit for their most significant position at 95% confidence of $E^2\,\mathrm{d}N/\mathrm{d}E = 3.51 \times 10^{-13}\,(E/\mathrm{TeV})^{-0.3}\,\mathrm{TeV\,cm^{-2}\,s^{-1}}$, in the energy range 300 GeV to 100 TeV, for the period from 2019 September 30 05:46:52 UTC to 2019 October 02 06:03:29 UTC. We note that this search covered a relatively large region of the sky, and thus had a large associated trial factor. A dedicated search at the position of AT2019dsg would be more sensitive, especially one that additionally targeted the longer period over which the central engine is active.

Radio analysis. The four radio spectral energy distributions (SEDs) for AT2019dsg can be described by synchrotron emission from a population of relativistic electrons. We assume that the electrons are accelerated into a power-law distribution in energy $\mathrm{d}N_e/\mathrm{d}\gamma \propto \gamma^{-p}$. We expect that the lowest-energy electrons emit their synchrotron radiation below the synchrotron self-absorption frequency with negligible free–free absorption, and in this case the shape of the radio SED is determined by just three free parameters, p, the magnetic field B and the source radius R:

$$F_{\nu,\mathrm{sync}}(t) \propto \frac{j_\nu(B(t),p)}{\kappa_\nu(B(t),p)}\left(1 - \mathrm{e}^{-\kappa_\nu R(t)}\right) \quad (1)$$

where j_ν and κ_ν are the emission and absorption coefficients, respectively. The normalization of equation (1) depends on the source geometry and the so-called microphysical parameters (ϵ_e, ϵ_B) which will be treated separately below. Similarly to the case of radio-emitting TDE ASASSN-14li[28,79], we might expect some steady radio emission from the host galaxy. This baseline flux density is parameterized as

$$F_{\nu,\mathrm{baseline}} = F_{\mathrm{baseline}}\left(\frac{\nu}{1.28\,\mathrm{GHz}}\right)^{\alpha_{\mathrm{baseline}}} \quad (2)$$

such that the total flux density is given by

$$F_{\nu,\mathrm{total}} = F_{\nu,\mathrm{baseline}} + F_{\nu,\mathrm{sync}} \quad (3)$$

The magnetic field and radius are allowed to change for each epoch, while F_{baseline}, $\alpha_{\mathrm{baseline}}$ and p are assumed to be constant during our radio observations.

Using equation (3) to describe the synchrotron spectrum, we apply a Markov chain Monte Carlo approach[80] to determine a posterior probability distribution of the electron power-law index, as well as the peak frequency (ν_{peak}) and peak flux density (F_{peak}) for each radio epoch (Extended Data Fig. 5). We allow the measurement variance to be underestimated by some fractional amount f (see, for example, ref. [81]).

The last epoch of VLA observations, which has the best coverage of the optically thin part of the radio SED, yields $p = 3.0 \pm 0.15$, and we use this as a Gaussian prior when fitting all data simultaneously. We use a flat (uninformative) prior for the other parameters and we cap $\alpha_{\mathrm{baseline}}$ at 0 and F_{baseline} at 0.1 mJy (because the baseline flux density should be optically thin, $\alpha < 0$, and cannot exceed the observed post-TDE radio flux density). For the time-independent parameters we find $F_{\mathrm{baseline}} = 0.09 \pm 0.01$ mJy, $\alpha_{\mathrm{baseline}} = -0.2 \pm 0.1$, $p = 2.9 \pm 0.1$ and $\ln f = -3.4$. We find no significant covariance between the baseline flux-density parameters and the peak frequency or peak flux density.

To estimate the radius and energy of the radio-emitting region from the posterior distribution of F_{peak}, ν_{peak} and p, we use the scaling relations from ref. [26]. These relations depend on the electron power-law index and we propagate the uncertainty on p into our estimates of equipartition radius R_{eq} and the equipartition energy E_{eq}. Additional assumptions for the geometry and the microphysical parameters are required. For the geometry of the outflow, our default model is two conical emitting regions with $\phi = 30°$, which yield an area-covering factor $f_A = 1 - \cos\phi = 0.13$ and a volume factor $f_V = 2/(3\tan\phi) = 1.15$ (here we follow the convention[26] that $f_A = 1$ and $f_V = 4/3$ parameterize a spherical outflow in the Newtonian limit).

The equipartition energy is obtained under the assumption that the system contains only electrons and magnetic fields (both uniformly distributed) and that the total energy is minimized for $E_B = (6/11)E_e$. However, we expect that protons carry the bulk of the energy and we parameterize this energy in protons by $\epsilon_e \equiv E_e/E_p$, with E_p the total energy in relativistic protons. After this adjustment, E_{eq} is increased by $(1 + 1/\epsilon_e)^{11/(13+2p)}$. Finally, for systems that are not in equipartition, the energy is larger by a factor[26] $(11/17)\eta^{-6/17} + (6/17)\eta^{11/17}$, with $\eta \equiv [\epsilon_B/(1-\epsilon_B)]/(6/11)$. Motivated by observations of gamma-ray burst afterglows[82,83], supernovae[25] and the relativistic TDE Swift J1644+57 (ref. [24]), we use $\epsilon_e = 0.1$ and $\epsilon_B = 10^{-3}$. From the equipartition magnetic field strength inferred from the first epoch of radio observation (Extended Data Fig. 5), we estimate that the cooling time of the electrons that emit at 10 GHz is 500 d. For the last epoch, the field strength has decreased by a factor of 3 and now the cooling time is an order of magnitude longer. We can thus conclude that, unless the magnetic field energy density is much higher than the equipartition value ($\epsilon_B/\epsilon_e \gg 1$), the observed slope of the optically thin part of the radio SEDs reflects the intrinsic power-law index of the electrons.

From our synchrotron analysis we also obtain the number density of relativistic electrons, which in turn yields a lower limit to the total particle density in the radio region. This estimate is relevant for the pp scenario of pion production, which requires a target density of at least $\sim 10^8\,\mathrm{cm^{-3}}$ to have sufficient optical depth. For the energy and radius of the last radio epoch, which was obtained a few days after the neutrino detection, we find an electron density of $10^{3.4\pm0.1}\,\mathrm{cm^{-3}}$ (Extended Data Fig. 5).

We note that there is no evidence of correlation between the X-ray and radio emission in AT2019dsg, in contrast to coupling found for ASASSN-14li[30]. Such a correlation would only be expected if the X-ray luminosity of AT2019dsg served as a tracer of disk power, and the rapid observed fading indicates that the observed X-ray emission in AT2019dsg is instead driven by either varying obscuration or temperature evolution.

Data availability

The data that support the plots within this paper and other findings of this study are available from https://github.com/robertdstein/at2019dsg, and at https://doi.org/10.5281/zenodo.4308124.

Code availability

Python scripts used to perform significant calculations, and to reproduce all figures, are available from https://github.com/robertdstein/at2019dsg, and at https://doi.org/10.5281/zenodo.4308124.

Received: 21 July 2020; Accepted: 16 December 2020;
Published online: 22 February 2021

References

1. Aartsen, M. G. et al. The IceCube Neutrino Observatory: instrumentation and online systems. *J. Instrum.* **12**, P03012 (2017).
2. Stein, R. IceCube-191001A—IceCube observation of a high-energy neutrino candidate event. *GCN Circ.* 25913 (2019).
3. Bellm, E. C. et al. The Zwicky Transient Facility: system overview, performance, and first results. *Publ. Astron. Soc. Pac.* **131**, 018002 (2019).
4. Kowalski, M. & Mohr, A. Detecting neutrino transients with optical follow-up observations. *Astropart. Phys.* **27**, 533–538 (2007).
5. Farrar, G. R. & Gruzinov, A. Giant AGN flares and cosmic ray bursts. *Astrophys. J.* **693**, 329–332 (2009).
6. Dai, L. & Fang, K. Can tidal disruption events produce the IceCube neutrinos? *Mon. Not. R. Astron. Soc.* **469**, 1354–1359 (2017).

7. Hayasaki, K. & Yamazaki, R. Neutrino emissions from tidal disruption remnants. *Astrophys. J.* **886**, 114 (2019).
8. Farrar, G. R. & Piran, T. Tidal disruption jets as the source of Ultra-High Energy Cosmic Rays. Preprint at https://arxiv.org/abs/1411.0704 (2014).
9. Senno, N., Murase, K. & Mészáros, P. High-energy neutrino flares from X-ray bright and dark tidal disruption events. *Astrophys. J.* **838**, 3 (2017).
10. Wang, X. Y. & Liu, R. Y. Tidal disruption jets of supermassive black holes as hidden sources of cosmic rays: explaining the IceCube TeV–PeV neutrinos. *Phys. Rev. D* **93**, 083005 (2016).
11. Lunardini, C. & Winter, W. High energy neutrinos from the tidal disruption of stars. *Phys. Rev. D* **95**, 123001 (2017).
12. Stein, R., Franckowiak, A., Necker, J., Gezari, S. & Velzen, S. V. Candidate counterparts to IceCube-191001A with ZTF. *Astron. Telegr.* 13160 (2019).
13. Graham, M. J. et al. The Zwicky Transient Facility: science objectives. *Publ. Astron. Soc. Pac.* **131**, 078001 (2019).
14. Nordin, J. et al. *TNS Astronomical Transient Report* 33340 (2019).
15. Nicholl, M. et al. ePESSTO+ classification of optical transients. *Astron. Telegr.* 12752 (2019).
16. van Velzen, S. et al. Seventeen tidal disruption events from the first half of ZTF survey observations: entering a new era of population studies. Preprint at https://arxiv.org/abs/2001.01409 (2020).
17. van Velzen, S. et al. Late-time UV observations of tidal disruption flares reveal unobscured, compact accretion disks. *Astrophys. J.* **878**, 82 (2019).
18. Mummery, A. & Balbus, S. A. The spectral evolution of disc dominated tidal disruption events. *Mon. Not. R. Astron. Soc.* **492**, 5655–5674 (2020).
19. McConnell, N. J. & Ma, C. P. Revisiting the scaling relations of black hole masses and host galaxy properties. *Astrophys. J.* **764**, 184 (2013).
20. Auchettl, K., Guillochon, J. & Ramirez-Ruiz, E. New physical insights about tidal disruption events from a comprehensive observational inventory at X-ray wavelengths. *Astrophys. J.* **838**, 149 (2017).
21. Wevers, T. et al. Black hole masses of tidal disruption event host galaxies II. *Mon. Not. R. Astron. Soc.* **487**, 4136–4152 (2019).
22. van Velzen, S. et al. The first tidal disruption flare in ZTF: from photometric selection to multi-wavelength characterization. *Astrophys. J.* **872**, 198 (2019).
23. Morlino, G. & Caprioli, D. Strong evidence for hadron acceleration in Tycho's supernova remnant. *Astron. Astrophys.* **538**, A81 (2012).
24. Eftekhari, T., Berger, E., Zauderer, B. A., Margutti, R. & Alexander, K. D. Radio monitoring of the tidal disruption event Swift J164449.3+573451. III. Late-time jet energetics and a deviation from equipartition. *Astrophys. J.* **854**, 86 (2018).
25. Horesh, A. et al. An early and comprehensive millimetre and centimetre wave and X-ray study of SN 2011dh: a non-equipartition blast wave expanding into a massive stellar wind. *Mon. Not. R. Astron. Soc.* **436**, 1258–1267 (2013).
26. Barniol Duran, R., Nakar, E. & Piran, T. Radius constraints and minimal equipartition energy of relativistically moving synchrotron sources. *Astrophys. J.* **772**, 78 (2013).
27. Polatidis, A. G. & Conway, J. E. Proper motions in compact symmetric objects. *Publ. Astron. Soc. Aust.* **20**, 69–74 (2003).
28. Alexander, K. D., Berger, E., Guillochon, J., Zauderer, B. A. & Williams, P. K. G. Discovery of an outflow from radio observations of the tidal disruption event ASASSN-14li. *Astrophys. J. Lett.* **819**, L25 (2016).
29. Krolik, J., Piran, T., Svirski, G. & Cheng, R. M. ASASSN-14li: a model tidal disruption event. *Astrophys. J.* **827**, 127 (2016).
30. Pasham, D. R. & van Velzen, S. Discovery of a time lag between the soft X-ray and radio emission of the tidal disruption flare ASASSN-14li: evidence for linear disk–jet coupling. *Astrophys. J.* **856**, 1 (2018).
31. Strotjohann, N. L., Kowalski, M. & Franckowiak, A. Eddington bias for cosmic neutrino sources. *Astron. Astrophys.* **622**, L9 (2019).
32. Hillas, A. M. The origin of ultra-high-energy cosmic rays. *Annu. Rev. Astron. Astrophys.* **22**, 425–444 (1984).
33. IceCube Collaboration et al. Multimessenger observations of a flaring blazar coincident with high-energy neutrino IceCube-170922A. *Science* **361**, eaat1378 (2018).
34. Blaufuss, E., Kintscher, T., Lu, L. & Tung, C. F. The next generation of IceCube real-time neutrino alerts. In *Proc. 36th International Cosmic Ray Conference (ICRC2019)* 1021 (PoS, 2019).
35. Murase, K., Guetta, D. & Ahlers, M. Hidden cosmic-ray accelerators as an origin of TeV–PeV cosmic neutrinos. *Phys. Rev. Lett.* **116**, 071101 (2016).
36. Stein, R. Search for neutrinos from populations of optical transients. In *Proc. 36th International Cosmic Ray Conference (ICRC2019)* 1016 (PoS, 2019).
37. Coughlin, M. W. et al. 2900 square degree search for the optical counterpart of short gamma-ray burst GRB 180523B with the Zwicky Transient Facility. *Publ. Astron. Soc. Pac.* **131**, 048001 (2019).
38. Stein, R. IceCube-200107A: IceCube observation of a high-energy neutrino candidate event. *GCN Circ.* 26655 (2020).
39. Masci, F. J. et al. The Zwicky Transient Facility: data processing, products, and archive. *Publ. Astron. Soc. Pac.* **131**, 018003 (2019).
40. Patterson, M. T. et al. The Zwicky Transient Facility Alert Distribution System. *Publ. Astron. Soc. Pac.* **131**, 018001 (2019).
41. Stein, R. & Reusch, S. *robertdstein/ampel_followup_pipeline: V1.1 Release* (Zenodo, 2020); https://doi.org/10.5281/zenodo.4048336
42. Nordin, J. et al. Transient processing and analysis using AMPEL: alert management, photometry, and evaluation of light curves. *Astron. Astrophys.* **631**, A147 (2019).
43. Mahabal, A. et al. Machine learning for the Zwicky Transient Facility. *Publ. Astron. Soc. Pac.* **131**, 038002 (2019).
44. Soumagnac, M. T. & Ofek, E. O. catsHTM: a tool for fast accessing and cross-matching large astronomical catalogs. *Publ. Astron. Soc. Pac.* **130**, 075002 (2018).
45. Gaia Collaboration et al. Gaia Data Release 2. Summary of the contents and survey properties. *Astron. Astrophys.* **616**, A1 (2018).
46. Tachibana, Y. & Miller, A. A. A morphological classification model to identify unresolved PanSTARRS1 sources: application in the ZTF real-time pipeline. *Publ. Astron. Soc. Pac.* **130**, 128001 (2018).
47. Chambers, K. C. et al. The Pan-STARRS1 Surveys. Preprint at https://arxiv.org/abs/1612.05560 (2016).
48. Wright, E. L. et al. The Wide-field Infrared Survey Explorer (WISE): mission description and initial on-orbit performance. *Astron. J.* **140**, 1868–1881 (2010).
49. Aartsen, M. G. et al. Time-integrated neutrino source searches with 10 years of IceCube data. *Phys. Rev. Lett.* **124**, 051103 (2020).
50. Steele, I. A. et al. The Liverpool Telescope: performance and first results. *Proc. SPIE* **5489**, https://doi.org/10.1117/12.551456 (2004).
51. Blagorodnova, N. et al. The SED Machine: a robotic spectrograph for fast transient classification. *Publ. Astron. Soc. Pac.* **130**, 035003 (2018).
52. Rigault, M. et al. Fully automated integral field spectrograph pipeline for the SEDMachine: pysedm. *Astron. Astrophys.* **627**, A115 (2019).
53. Fremling, C. et al. PTF12os and iPTF13bvn. Two stripped-envelope supernovae from low-mass progenitors in NGC 5806. *Astron. Astrophys.* **593**, A68 (2016).
54. van Velzen, S. On the mass and luminosity functions of tidal disruption flares: rate suppression due to black hole event horizons. *Astrophys. J.* **852**, 72 (2018).
55. Roming, P. W. A. et al. The Swift Ultra-Violet/Optical Telescope. *Space Sci. Rev.* **120**, 95–142 (2005).
56. Gehrels, N. et al. The Swift Gamma-Ray Burst Mission. *Astrophys. J.* **611**, 1005–1020 (2004).
57. van Velzen, S., Mendez, A. J., Krolik, J. H. & Gorjian, V. Discovery of transient infrared emission from dust heated by stellar tidal disruption flares. *Astrophys. J.* **829**, 19 (2016).
58. Lu, W., Kumar, P. & Evans, N. J. Infrared emission from tidal disruption events—probing the pc-scale dust content around galactic nuclei. *Mon. Not. R. Astron. Soc.* **458**, 575–581 (2016).
59. Miller, J. S. & Stone, R. P. S. *The Kast Double Spectrograph.* Technical Report No. 66 (Lick Observatory, 1993).
60. Oke, J. B. et al. The Keck Low-Resolution Imaging Spectrometer. *Publ. Astron. Soc. Pac.* **107**, 375–385 (1995).
61. Garcia-Rissmann, A. et al. An atlas of calcium triplet spectra of active galaxies. *Mon. Not. R. Astron. Soc.* **359**, 765–780 (2005).
62. Burrows, D. N. et al. The Swift X-Ray Telescope. *Space Sci. Rev.* **120**, 165–195 (2005).
63. Jansen, F. et al. XMM-Newton Observatory. I. The spacecraft and operations. *Astron. Astrophys.* **365**, L1–L6 (2001).
64. HI4PI Collaboration et al. HI4PI: a full-sky H I survey based on EBHIS and GASS. *Astron. Astrophys.* **594**, A116 (2016).
65. Arnaud, K. A. in *Astronomical Data Analysis Software and Systems V* (eds Jacoby, G. H. & Barnes, J.) 17 (Astronomical Society of the Pacific, 1996).
66. Zwart, J. T. L. et al. The Arcminute Microkelvin Imager. *Mon. Not. R. Astron. Soc.* **391**, 1545–1558 (2008).
67. Hickish, J. et al. A digital correlator upgrade for the Arcminute MicroKelvin Imager. *Mon. Not. R. Astron. Soc.* **475**, 5677–5687 (2018).
68. Perrott, Y. C. et al. AMI galactic plane survey at 16 GHz—II. Full data release with extended coverage and improved processing. *Mon. Not. R. Astron. Soc.* **453**, 1396–1403 (2015).
69. McMullin, J. P., Waters, B., Schiebel, D., Young, W. & Golap, K. in *Astronomical Data Analysis Software and Systems XVI* (eds Shaw, R. A. et al.) 127 (Astronomical Society of the Pacific, 2007).
70. Atwood, W. B. et al. The Large Area Telescope on the Fermi Gamma-ray Space Telescope mission. *Astrophys. J.* **697**, 1071–1102 (2009).
71. Wood, M. et al. Fermipy: an open-source Python package for analysis of Fermi-LAT Data. In *Proc. 35th International Cosmic Ray Conference (ICRC2017)* 824 (PoS, 2017).
72. Garrappa, S. & Buson, S. Fermi-LAT gamma-ray observations of IceCube-191001A. *GCN Circ.* 25932 (2019).
73. The Fermi-LAT collaboration. Fermi Large Area Telescope Fourth Source Catalog. *Astrophys. J. Suppl. Ser.* **247**, 33 (2020).
74. Pursimo, T. et al. The Micro-Arcsecond Scintillation-Induced Variability (MASIV) survey. III. Optical identifications and new redshifts. *Astrophys. J.* **767**, 14 (2013).

75. Garrappa, S., Buson, S. & Fermi-LAT Collaboration. Fermi-LAT gamma-ray observations of IceCube-191001A. *GCN Circ.* 25932 (2019).
76. Diltz, C., Böttcher, M. & Fossati, G. Time dependent hadronic modeling of flat spectrum radio quasars. *Astrophys. J.* **802**, 133 (2015).
77. Gao, S., Fedynitch, A., Winter, W. & Pohl, M. Modelling the coincident observation of a high-energy neutrino and a bright blazar flare. *Nat. Astron.* **3**, 88–92 (2019).
78. Ayala, H. IceCube-191001A: HAWC follow-up. *GCN Circ.* 25936 (2019).
79. van Velzen, S. et al. A radio jet from the optical and x-ray bright stellar tidal disruption flare ASASSN-14li. *Science* **351**, 62–65 (2016).
80. Foreman-Mackey, D., Hogg, D. W., Lang, D. & Goodman, J. emcee: the MCMC Hammer. *Publ. Astron. Soc. Pac.* **125**, 306 (2013).
81. Guillochon, J. et al. MOSFiT: Modular Open Source Fitter for Transients. *Astrophys. J. Suppl. Ser.* **236**, 6 (2018).
82. Granot, J. & van der Horst, A. J. Gamma-ray burst jets and their radio observations. *Publ. Astron. Soc. Aust.* **31**, e008 (2014).
83. Fong, W., Berger, E., Margutti, R. & Zauderer, B. A. A decade of short-duration gamma-ray burst broadband afterglows: energetics, circumburst densities, and jet opening angles. *Astrophys. J.* **815**, 102 (2015).

Acknowledgements

We thank C. Lunardini, A. MacFadyen, B. Metzger, A. Mummery, A. Pizzuto, N. Stone, A. Taylor and W. Winter for discussions. We also thank the IceCube Collaboration for publishing high-energy neutrino alerts. We thank S. Digel, K. Fang, D. Horan, M. Kerr, V. Paliya and J. Racusin for feedback provided during a Fermi collaboration review. R.S. is grateful to NYU for facilitating a visit to develop this work. M.K. is grateful for the hospitality received from Columbia University and NYU during a sabbatical visit. This work was supported by the Initiative and Networking Fund of the Helmholtz Association through the Young Investigator Group programme (A.F.). S.v.V. is supported by the James Arthur Postdoctoral Fellowship. This research was partially supported by the Australian Government through the Australian Research Council's Discovery Projects funding scheme (project DP200102471). The work of M.B. is supported through the South African Research Chair Initiative of the National Research Foundation and the Department of Science and Innovation of South Africa, under SARChI Chair grant no. 64789. Any opinion, finding and conclusion or recommendation expressed in this material is that of the authors and the NRF does not accept any liability in this regard. A.H. acknowledges support by the I-Core Program of the Planning and Budgeting Committee and the Israel Science Foundation. The UCSC transient team is supported in part by NSF grant AST-1518052, NASA/Swift grant 80NSSC19K1386, the Gordon & Betty Moore Foundation, the Heising-Simons Foundation and a fellowship from the David and Lucile Packard Foundation to R.J.F. V.Z.G. is a Moore–Sloan, WRF Innovation in Data Science and DIRAC Fellow. A.G.-Y.s research is supported by the EU via ERC grant no. 725161, the ISF GW Excellence Center, an IMOS space infrastructure grant and BSF/Transformative and GIF grants, as well as the Benoziyo Endowment Fund for the Advancement of Science, the André Deloro Institute for Advanced Research in Space and Optics, the Veronika A. Rabl Physics Discretionary Fund, Paul and Tina Gardner, Yeda-Sela and the WIS-CIT joint research grant; A.G.-Y. is the recipient of the Helen and Martin Kimmel Award for Innovative Investigation. M.R. has received funding from the European Research Council (ERC) under the European Union's Horizon 2020 research and innovation programme (grant agreement no. 759194-USNAC). The work of D.S. was carried out at the Jet Propulsion Laboratory, California Institute of Technology, under a contract with NASA. The work of S.R. was supported by the Helmholtz Weizmann Research School on Multimessenger Astronomy, funded through the Initiative and Networking Fund of the Helmholtz Association, DESY, the Weizmann Institute, the Humboldt University of Berlin and the University of Potsdam. This work is based on observations obtained with the Samuel Oschin telescope 48-inch and the 60-inch telescope at the Palomar Observatory as part of the ZTF project. ZTF is supported by the National Science Foundation under grant no. AST-1440341 and a collaboration including Caltech, IPAC, the Weizmann Institute for Science, the Oskar Klein Center at Stockholm University, the University of Maryland, the University of Washington, Deutsches Elektronen-Synchrotron and Humboldt University, Los Alamos National Laboratories, the TANGO Consortium of Taiwan, the University of Wisconsin at Milwaukee and Lawrence Berkeley National Laboratories. Operations are conducted by COO, IPAC and UW. SED Machine is based upon work supported by the National Science Foundation under grant no. 1106171. The National Radio Astronomy Observatory is a facility of the National Science Foundation operated under cooperative agreement by Associated Universities, Inc. The MeerKAT telescope is operated by the South African Radio Astronomy Observatory, which is a facility of the National Research Foundation, an agency of the Department of Science and Innovation. The work was supported by the GROWTH project funded by the National Science Foundation Partnership in International Research and Education program under grant no. 1545949. GROWTH is a collaborative project between the California Institute of Technology (United States), Pomona College (United States), San Diego State University (United States), Los Alamos National Laboratory (United States), University of Maryland College Park (United States), University of Wisconsin at Milwaukee (United States), Tokyo Institute of Technology (Japan), National Central University (Taiwan), Indian Institute of Astrophysics (India), Inter-University Center for Astronomy and Astrophysics (India), Weizmann Institute of Science (Israel), The Oskar Klein Centre at Stockholm University (Sweden) and Humboldt University (Germany). The Liverpool Telescope is operated on the island of La Palma by Liverpool John Moores University in the Spanish Observatorio del Roque de los Muchachos of the Instituto de Astrofísica de Canarias with financial support from the UK Science and Technology Facilities Council. Research at Lick Observatory is partially supported by a gift from Google. The Fermi-LAT Collaboration acknowledges support for LAT development, operation and data analysis from NASA and DOE (United States), CEA/Irfu and IN2P3/CNRS (France), ASI and INFN (Italy), MEXT, KEK and JAXA (Japan) and the K.A. Wallenberg Foundation, the Swedish Research Council and the National Space Board (Sweden). Science analysis support in the operations phase from INAF (Italy) and CNES (France) is also acknowledged. This work was performed in part under DOE contract DE-AC02-76SF00515. IceCube Neutrino Observatory is a facility of the National Science Foundation operated at the US Amundsen–Scott South Pole Station under the US Antarctic Program.

Author contributions

R.S. first identified AT2019dsg as a candidate neutrino source, performed the neutrino analysis and was the primary author of the manuscript. M.K., R.S. and S.v.V. developed the multizone model. G.R.F., M.K. and R.S. performed the neutrino modelling. A.F., J. Necker, R.S. and S.R. scheduled and analysed ZTF ToO observations. J.C.A.M.-J. and S.v.V. contributed the VLA observations. A.H., R.J.F. and I.S. contributed the AMI-LA observations. M.F.B., M.B., R.J.F., J.C.A.M.-J. and P.W. contributed the MeerKAT observations. S. Gezari and S.v.V. requested and reduced the Swift-UVOT data. D.A.P. and K.T. contributed the Liverpool Telescope observations. S.B.C., S.F. and S. Gezari performed X-ray observations and data analysis. S. Garrappa analysed Fermi gamma-ray data. S.R. and S.v.V. analysed the ZTF data. J.B., E.C.B., R.B., S.B.C., V.C., M.F., V.Z.G., A.G., M.J.G, G.H., M.M.K., T.K., R.R.L., A.A.M, F.J.M., H.R., B.R., D.L.S. and M.T.S contributed to the implementation of ZTF. T.A., I.A., M.W.C., M.M.K. and L.P.S. enabled ZTF ToO observations. A.D., R.J.F., M.J.G., S. Gezari, E.H., T.H., M.M.K., C.D.K., M.R., C.R.-B., D.S, C.W. and Y.Y. contributed to spectroscopic observations and data reduction. R.S. developed the ToO analysis pipeline. V.B., J. Nordin and J.v.S. developed AMPEL, and contributed to the ToO analysis infrastructure. A.G.-Y., A.K.H.K. and J.S. contributed to the manuscript and discussions. All authors reviewed the contents of the manuscript.

Competing interests

The authors declare no competing interests.

Additional information

Extended data is available for this paper at https://doi.org/10.1038/s41550-020-01295-8.

Supplementary information The online version contains supplementary material available at https://doi.org/10.1038/s41550-020-01295-8.

Correspondence and requests for materials should be addressed to R.S., S.v.V. or M.K.

Peer review information *Nature Astronomy* thanks Kimitake Hayasaki and the other, anonymous, reviewer(s) for their contribution to the peer review of this work.

Reprints and permissions information is available at www.nature.com/reprints.

Publisher's note Springer Nature remains neutral with regard to jurisdictional claims in published maps and institutional affiliations.

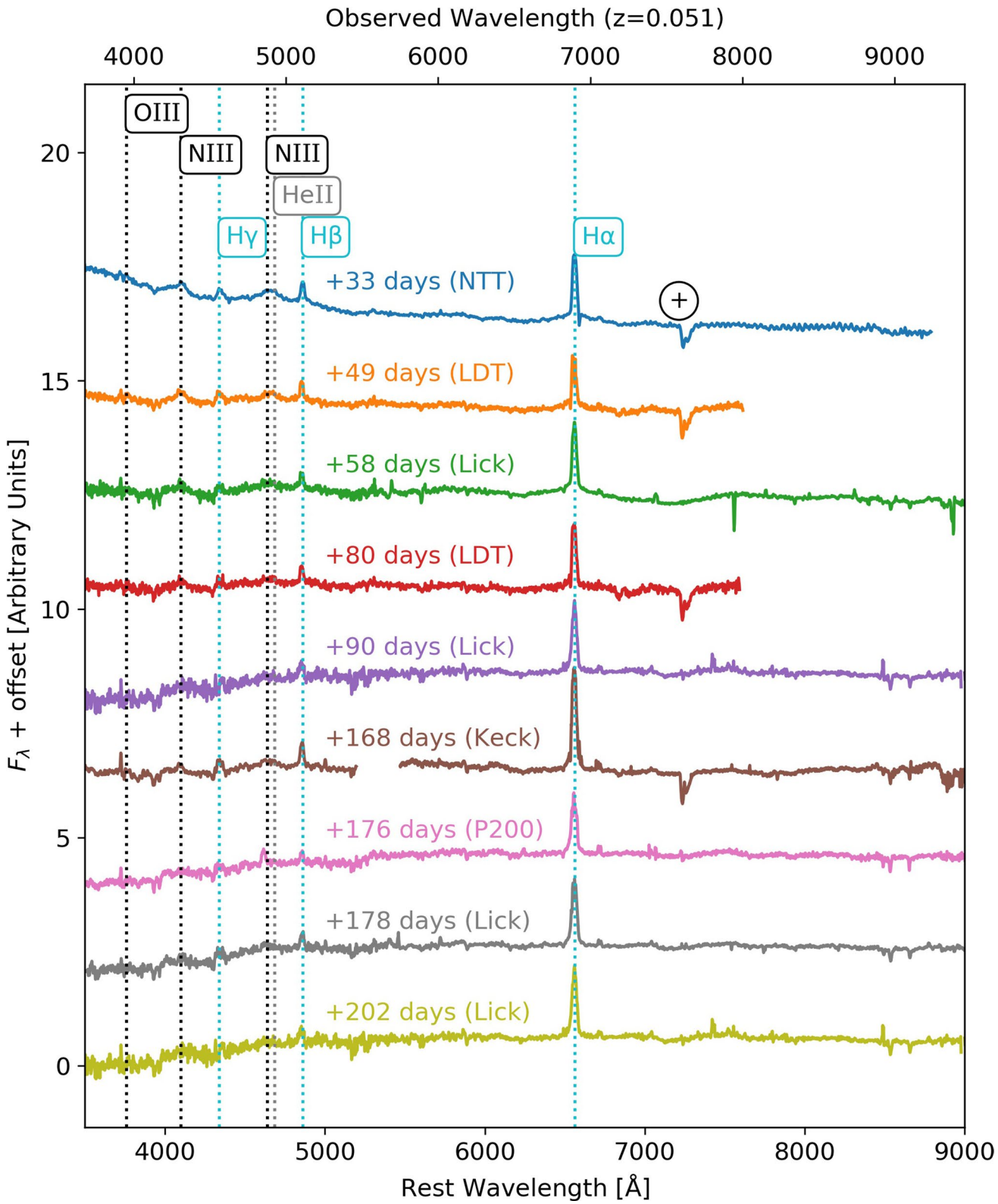

Extended Data Fig. 1 | Spectroscopic evolution of AT2019dsg. The public classification spectrum taken with the NTT[15] is plotted in blue, along with later spectra from LDT, Lick, Keck and P200. Each is plotted in arbitrary units, offset for display purposes. The Balmer lines are highlighted in cyan, the HeII lines in gray, and the Bowen fluorescence lines (OIII at 3760Å, NIII at 4100Å and 4640Å) in black. Telluric lines are marked with +.

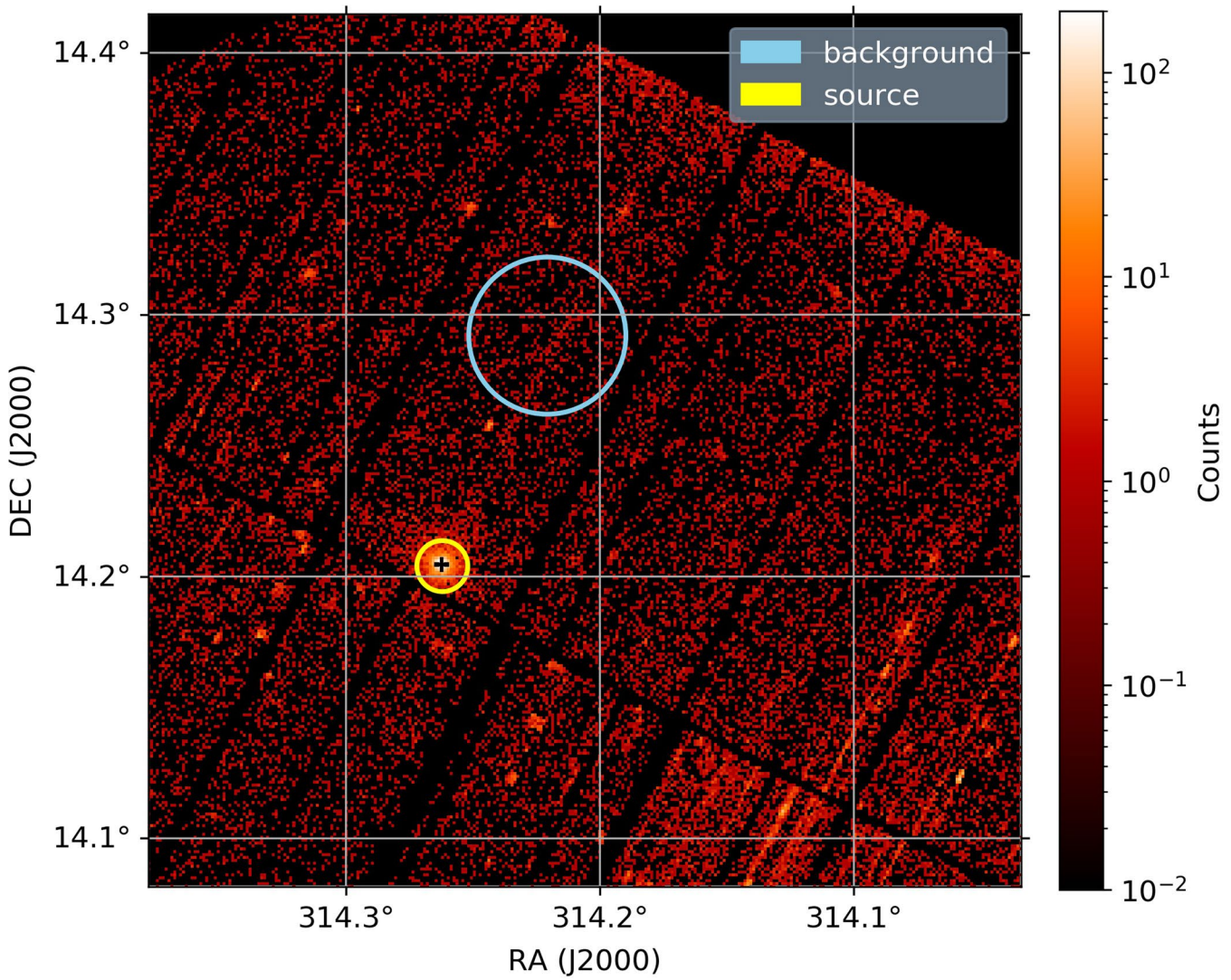

Extended Data Fig. 2 | X-ray count map from *XMM-Newton*. The image was taken 50 days after discovery. The green circle indicates the source region, while the red circular region was used to measure the background. The best-fit position derived from optical observations is spatially-coincident with the center of the X-ray source region.

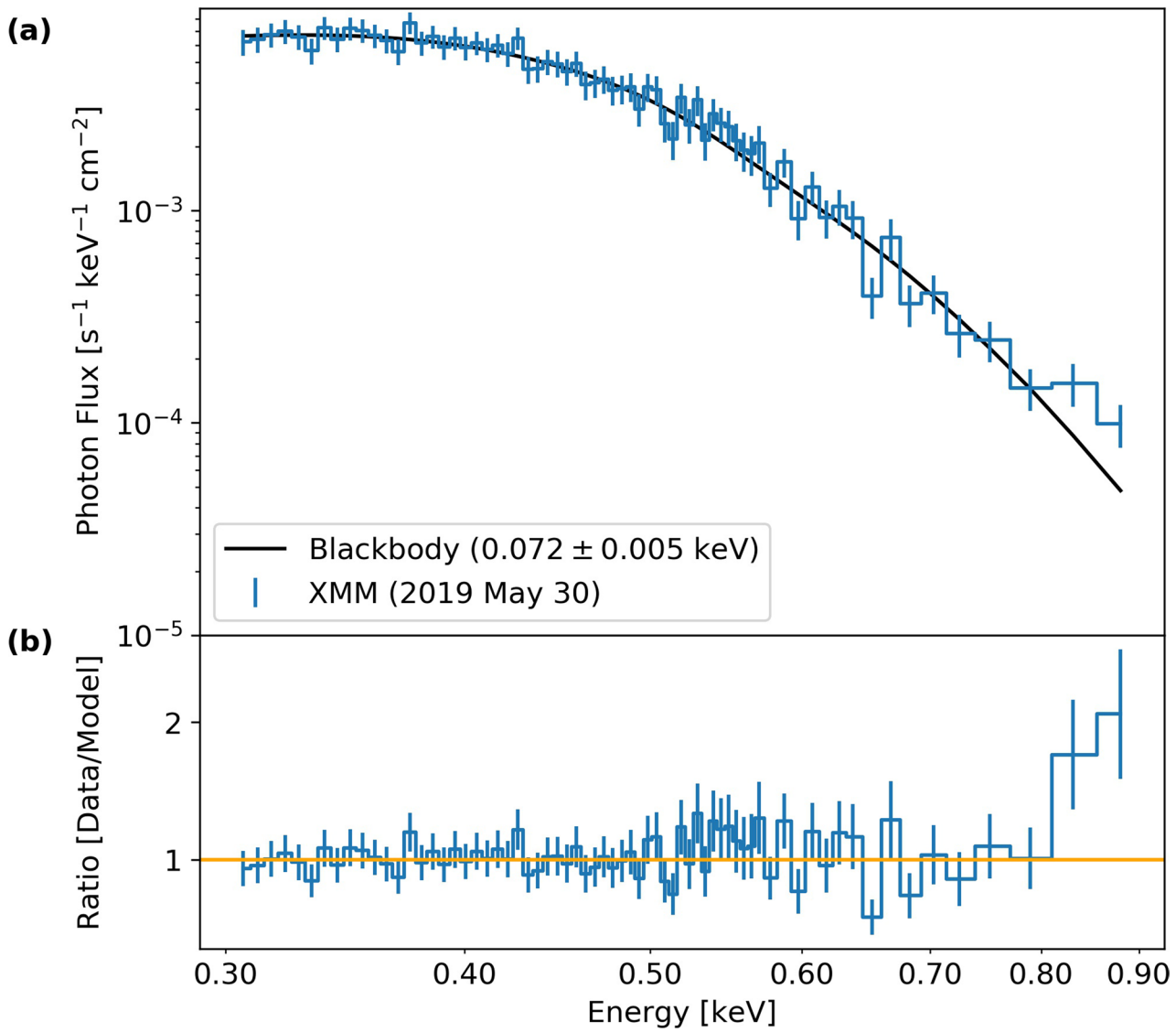

Extended Data Fig. 3 | Soft X-ray spectrum of AT2019dsg. Panel (**a**) shows the photon flux as a function of energy in blue, from the XMM Newton spectrum taken on 2019 May 30. The spectrum was fitted with an absorbed disk blackbody model, shown in black. Panel (**b**) shows the ratio of the data to the model, with the horizontal orange line indicating unity. Error bars represent 1σ intervals.

Δt [days]	$F_{\rm peak}$ [mJy]	$\nu_{\rm peak}$ [GHz]
42	0.41 ± 0.04	14.8 ± 1.0
70	0.71 ± 0.04	12.0 ± 0.5
120	1.20 ± 0.04	9.4 ± 0.3
178	1.24 ± 0.04	5.4 ± 0.1

Extended Data Fig. 4 | Peak frequency and peak flux density of the radio observations. The time (Δt) is measured in the observer frame relative to MJD 58582.8, the date of discovery for AT2019dsg.

		equipartition: $E_e/E_B = 11/6$ (no protons)				fiducial model: $\epsilon_e = 0.1$; $\epsilon_B = 10^{-3}$			
	Δt [days]	$R_{\rm eq}$ [erg]	$E_{\rm eq}$ [cm]	$B_{\rm eq}$ [G]	$n_{e,\rm eq}$ [cm^{-3}]	R [cm]	E [erg]	B [G]	n_e [cm^{-3}]
Conical: f_A=0.13 f_V=1.15	42	16.29(0.02)	47.9(0.1)	−0.27(0.05)	3.5(0.1)	16.18(0.03)	49.4(0.1)	−0.68(0.05)	4.4(0.1)
	70	16.47(0.02)	48.3(0.1)	−0.36(0.04)	3.3(0.1)	16.37(0.02)	49.7(0.1)	−0.78(0.04)	4.2(0.1)
	120	16.68(0.02)	48.7(0.1)	−0.49(0.04)	3.0(0.1)	16.57(0.02)	50.1(0.1)	−0.91(0.04)	3.9(0.1)
	178	16.93(0.02)	48.9(0.1)	−0.73(0.05)	2.6(0.1)	16.82(0.02)	50.3(0.1)	−1.16(0.04)	3.4(0.1)
Spherical: f_A=1 f_V=4/3	42	15.92(0.02)	47.4(0.1)	−0.00(0.04)	4.0(0.1)	15.81(0.03)	48.8(0.1)	−0.41(0.04)	4.9(0.1)
	70	16.10(0.02)	47.8(0.1)	−0.10(0.04)	3.8(0.1)	16.00(0.02)	49.2(0.1)	−0.52(0.04)	4.7(0.1)
	120	16.31(0.02)	48.2(0.1)	−0.22(0.04)	3.6(0.1)	16.20(0.02)	49.6(0.1)	−0.65(0.04)	4.4(0.1)
	178	16.56(0.02)	48.4(0.1)	−0.47(0.04)	3.1(0.1)	16.45(0.02)	49.8(0.1)	−0.89(0.04)	3.9(0.1)

Extended Data Fig. 5 | Properties of radio-emitting region. These values are inferred from the synchrotron peak flux and peak frequency (see Extended Data Fig. 4), where R is the region radius, E is the non-thermal energy, B is the magnetic field strength and n_e is the density of non-thermal electrons. Except for Δt, all quantities are reported as $\log_{10}$ with the uncertainty (68% CL) listed in brackets.

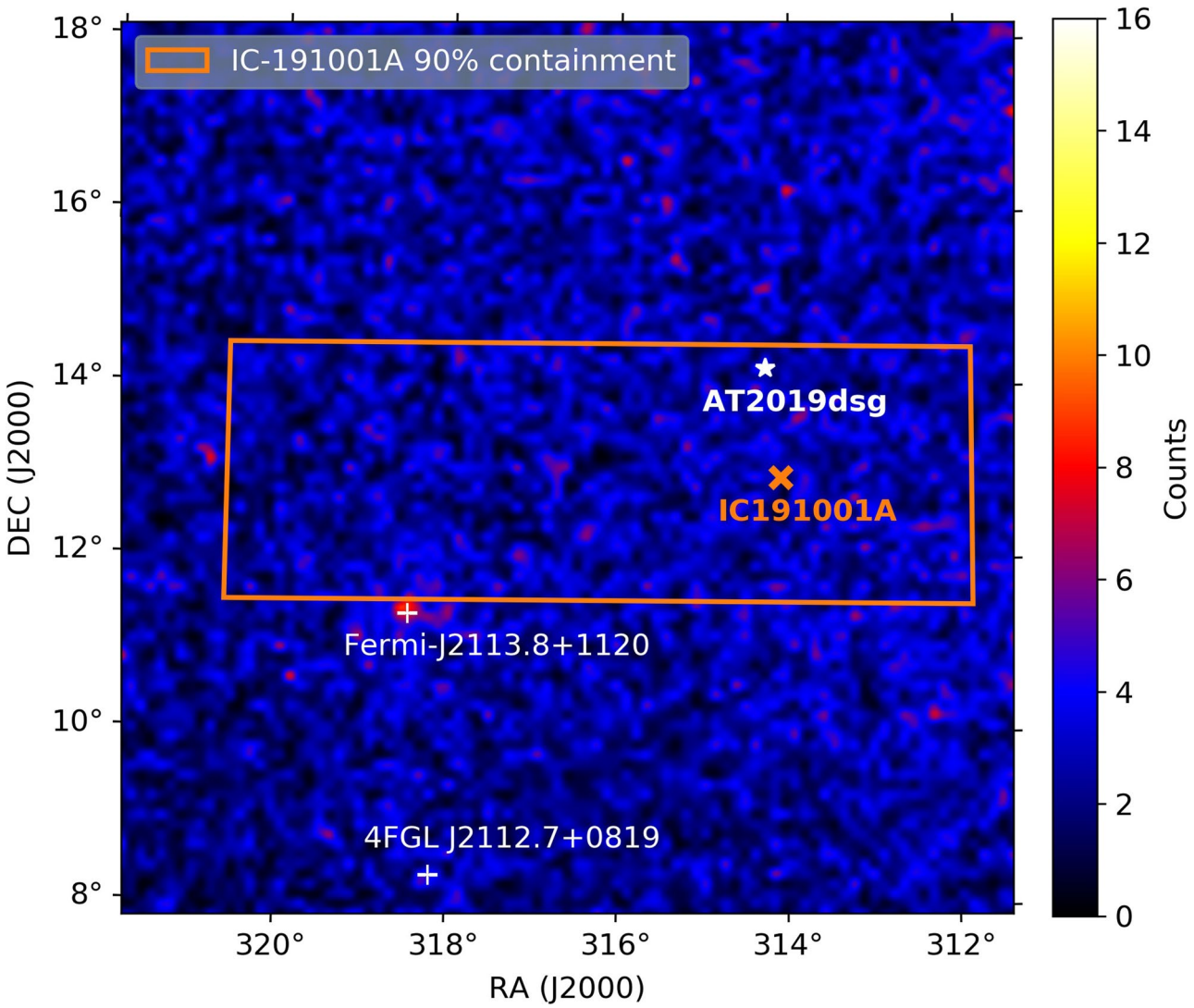

Extended Data Fig. 6 | LAT count map of the Region Of Interest (ROI). The map shows the integrated search period G3, showing the IC191001A 90% localisation region in orange. The position of AT2019dsg is marked by a white star. The neutrino best-fit position is marked with a orange '×'. Two gamma-ray sources are significantly detected ($\geq 5\,\sigma$) in the ROI but outside the neutrino uncertainty region as marked with white crosses. There is no excess consistent with the position of AT2019dsg.

Interval	MJD Start	MJD Stop	UL [erg cm^{-2} s^{-1}]
G1	58577	58707	2.6×10^{-12}
G2	58707	58807	1.2×10^{-11}
G3	58577	58879	2.0×10^{-12}

Extended Data Fig. 7 | Gamma-ray energy flux upper-limits for AT2019dsg. The values are derived assuming a point-source with power-law index Γ=2.0 at the position of AT2019dsg, integrated over the analysis energy range 0.1-800 GeV.

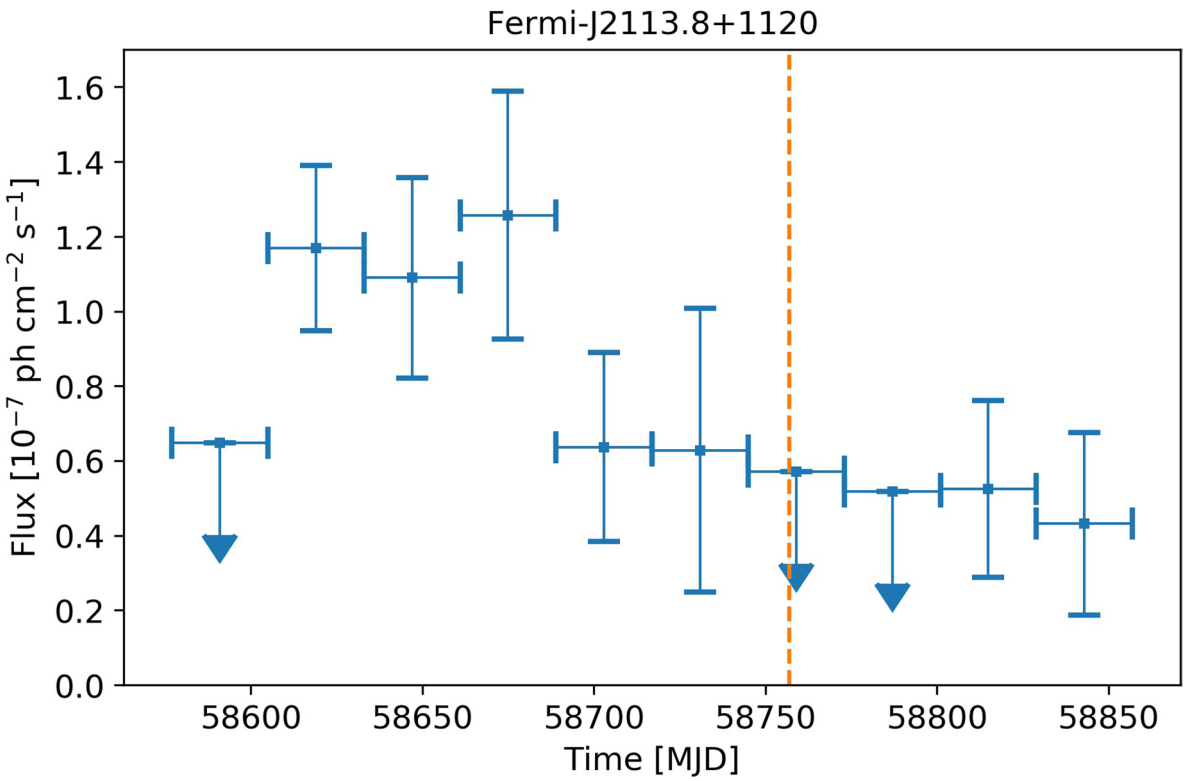

Extended Data Fig. 8 | LAT lightcurve for *Fermi*-J2113.8+1120. The flux is derived in the 0.1-800 GeV energy range for the source during the time interval G3, with evenly spaced binning of 28 days. Vertical error bars represent 1σ intervals, horizontal bars denote bin width. 2σ upper limits are shown for bins with TS≤9. The orange dashed vertical line marks the arrival time of IC-191001A. Since this source lies outside the reported 90% error region (see Extended Data Fig. 6), and given that the LAT lightcurve shows no obvious correlation with the neutrino arrival time, we conclude that it is unlikely to be associated with the neutrino.